Journal of Modern Materials
ISSN: 2456-4834
Volume 12, Issue 1, pp. 7-17, 2025
DOI: https://doi.org/10.21467/jmm.12.1.7-17

RESEARCH ARTICLE

Synthesis and Characterization of Tellurium Microtubes

Mohammed Kars[1, 2*], Adrian Gómez Herrero[3], Thierry Roisnel[4]

[1]Faculté de Chimie, Laboratoire Sciences des matériaux, Université des Sciences et de la Technologie Houari-Boumediene, USTHB, Algérie

[2]Département de Physique, Laboratoire de Physique Théorique et Interaction Rayonnement Matière, Université Blida1, Algérie

[3]Centro de Microscopia Electrónica, Universidad Complutense, 28040 Madrid, Spain

[4]CNRS, ISCR (Institut des Sciences Chimiques de Rennes), Université de Rennes 1, France

*Corresponding Author's e-mail: mkarsdz@yahoo.fr

Received: 29 March 2024 / Revised: 30 December 2024 / Accepted: 12 February 2025 / Published: 13 February 2025

ABSTRACT

Tellurium (*Te*) is a potential material for multiple applications due to its distinct features, including its anisotropic crystal structure and narrow bandgap energy. In this work, we use the chemical vapor transport reaction (*CVT*) method to synthesize tellurium microtubes (*Te MTs*) with hexagonal and rectangular cross-sections. The structure and composition of the *Te MTs* were analyzed using characterization methods such as, *X*-ray powder diffraction *(XRD),* selected-area electron diffraction (*SAED*), and energy-dispersive *X*-ray spectroscopy *(EDS*). Furthermore, computational techniques such as density functional theory *(DFT)* computations were utilized to examine the electronic and the optical properties of bulk *Te.*

Keywords: Tellurium Microtubes, Electronic microscopy, DFT.

1 Introduction

Tellurium (*Te*) is a *p*-type semiconductor with a narrow bandgap energy (0.33 eV) and a significantly anisotropic crystal structure formed by the parallel assembly of different infinite chains. These chains generate a hexagonal lattice with significant chirality, bound by weak van der Waals (*vdW*) interactions. *Te* exhibits a range of captivating physical features, in particular photoconductivity [1], non-linear optical response [2], strong thermoelectric [3], piezoelectric effects [4], and more, making it suitable for use in electronic and optoelectronic devices [5], [6]. Due to its anisotropic nature, tellurium easily forms *1D* nanostructures, such as nanowires, nanobelts, and nanotubes (*NTs*), as well as *Te* microtubes (*MTs*). These nano/microstructures have possible uses in multiple domains, including biology [7], catalysis, nano [8], [9], gas sensors [10], and advanced applications [11], [12]. It is then critical to develop a controllable approach for producing tellurium (*Te*) nano- and microstructures with adjustable morphology and characteristics. Many approaches, such as physical evaporation, microwave-assisted processes, photothermal techniques, electrochemical deposition, and more, have been developed to synthesize nanocrystalline *Te* of various morphologies [13]-[20]. However, the most common growth strategy is the solution-phase technique suggested by B. Mayers *et al.* [15].

Very recently, progress in *2D* material synthesis technology has positioned tellurium as an emerged single-element *2D* material known as tellurene, with promising applications in advanced electronic and optoelectronic devices. These applications include complementary metal-oxide-semiconductor (*CMOS*) technologies, electric-field transistors (*FETs*), and van der Waals heterojunction (*vdWH*) [21]-[24]. The *Te MTs* are commonly produced by hydrothermal, solvothermal, and a basic physical evaporation approach; however, they have received comparatively less attention than tellurium nanotubes (*NTs*) [17], [25]-[27]. In this study, tellurium *MTs* with hexagonal and rectangular cross-sections were synthesized via a chemical

vapor transport process (*CVT*). The *MTs* structures were investigated using powder diffraction (*XRD*), selected-area electron diffraction (*SAED*), and energy-dispersive spectroscopy (*EDS*). In addition, tellurium crystals obtained from the same preparation were examined using computational methods with *CASTEP* and single-crystal *X*-ray diffraction.

2 Research Methodology

MTs of tellurium were obtained during our investigation in the *Bi-Nb-Te* system. A mixture of the elements *Bi*, *Nb*, and *Te* in a 1:1:2 molar ratio, was sealed and heated in an evacuated quartz tube with I_2 (<5 mg/cm^3) as a transport agent. The temperature was slowly increased to 400°C and kept for 48 hours to reduce thermal shock, followed by gradual increases to 1000°C for 10 days. The temperature was then slowly cooled at a rate of 50°C/hour to reach room temperature. In the resulting product, in addition to the *MTs* of tellurium, we also observed microplates and fibers with compositions close to $NbTe_3$, as well as crystals of elemental *Te* at the cooled end of the tube. Powder *X*-ray diffraction (*XRD*) was collected using a *Philips Panalytical X'pert MRD* diffractometer at room temperature with *Cu Ka1* radiation (λ = 1.54056 Å). The structure and phase identification were performed using the software *Match3* [28]. Single crystal data were collected using a *X*-ray diffractometer *SMART-APEX CCD* with monochromatic *Mo Ka* radiation (λ = 0.71071 Å). The reflection intensities were integrated using *SAINT* [29], and empirical absorption correction using *SADABS* [30] was applied. The crystal structure was first solved using *Superflip* [31] and further refined using the *JANA2006* program [32]. Molecular visualization was achieved using the *Diamond* program [33]. Table 1 displays detailed information regarding the structure refinement and results.

Table 1: *Single crystal data and structure refinement details for tellurium*

Formula	Te
Molar mass (g.mol^{-1})	127.60
Space group (SG)	$P3_121$
Z	3
Unit cell dimensions (Å)	a = 4.4432(3) ; c = 5.9346(4)
Volume (Å^3)	101.464 (10)
Calculated density ($g.cm^{-3}$)	6.265
Absorption coefficient (mm^{-1})	21.170
Angular range $\Theta(^o)$	5.3-40.8
Index ranges	$-8<h<8$; $-7<k<8$; $-10<l<10$
R_{int}	0.0556
Total recorded reflections	4294
Reflections with $I > 3\sigma(I)$	425
T_{min}/T_{max}	0.049/0.120
Data / GOF on F^2	9 / 1.74
$(R/R_w)_{obs}$ (%)	0.0196/ 0.0270
$(R/R_w)_{all}$ (%)	0.0196/ 0.0270
$\Delta\rho_{max}$, $\Delta\rho_{min}$ (e^-/Å^3)	1.09, -1.61
d_{Exp} : bond lengths (Å)	2.8360(4)

A JEOL JSM 6400 was used for *SEM* observations, and a camera microprobe equipped with a 1µm probe working at 20 kV and 12 mA was used for *EPMA* analysis. High-resolution *TEM (HRTEM)* images were obtained using a *JEM 3000 F* microscope having a point resolution of 0.17 nm coupled with an *INCA* Microanalysis Suite. For *TEM* analysis, samples were scraped off the substrate surface, crushed, and finally

dispersed with ultrasound in butanol. To support the crystallites, a small amount of the suspension was placed onto a copper grid covered with a porous carbon film.

The plane-wave pseudopotential approach [34] executed in the *Cambridge Sequential Total Energy Package* (*CASTEP*) Code from the *Accelrys Material Studio program* [35] was used for all *DFT* calculations. The exchange and correlation interactions were modeled using the *GGA-RPBE* (*Revised Perdew-Burke-Ernzerhof*) scheme [36] and the interactions between the valence electrons and the ion core were characterized by the norm-conserving approach. In tellurium bulk, the *Heyd–Scuserian–Ernzerhorf HSE03* hybrid functional [37] was used for accurately determining the band gap. A plane-wave basis set with a cut-off energy of 500 eV was established, and a dense *k*-mesh of 15x15x1 sampling using the *Monkhorst–Pack* technique was applied for optimization and calculations in *Brillouin* zone integration. Under self-consistent conditions, the maximum displacements were set at 5.10^{-4} Å, the stress limitations at 2.10^{-2} GPa, and the total energy per atom was required to be smaller than 5.10^{-6} eV. The calculations considered the valence electrons from the $4d^{10}5s^{2}5p^{4}$ orbitals of tellurium. Table 2 provides additional details on the optimized structural parameters and optical properties obtained using *HSE03*.

Table 2: *Structural optimization parameters and selected optical properties for tellurium*

Optimized lattice cell (*Å*)	a = 4.5881 ; c = 5.9395
Volume ($Å^3$)	108.280
s	1.95
p	4.05
d	0.00
Total	6.00
Charge (*e*)	0.00
Mulliken population : *MP*	0.07
Bond lengths (*Å*) : d_{Calc}	2.8914
Final Energy (*eV*) : E_F	-662.9183
Cohesive energy (*eV*) : E_{Coh}	-2.92
Bandgap (*eV*) : E_G	0.371
$\varepsilon_1(0)$: Dielectric function	28.6 ($\perp c$) ; 42.5 ($\|\|c$)
$\eta(0)$: Refractive index	5.35 ($\perp c$) ; 6.52 ($\|\|c$)
$\Delta n = ne - no$	-1.17
Lf : Loss function (*eV*)	14.3 ($\perp c$) ;18.4 ($\|\|c$)

3 Results and Discussion

Tellurium's crystal structure consists of covalently linked *Te* atoms assembled in helical chains running parallel to the c-axis. As seen in Figure *1a* and *1b,* these chains are connected through *vdW* forces to create the hexagonal lattice. Each *Te* atom forms covalent bonds with four (04) atoms in adjacent spiral chains and two (02) nearest atoms in the same spiral chain. This tendency could lead to crystals growing preferentially along the trigonal axis. The measured *Te-Te* distance of about 2.8359 (4) Å is in good agreement with the 2.8345 (8) Å value published by C. Adenis *et al.* [38].

3.1 Theoretical results

Selected optimized structural parameters and optical properties of tellurium are presented in Table 2. The optimized lattice parameters are in good agreement with our experimental findings and previous theoretical computations [39]-[43]. It was observed that only the *a* parameter is slightly overestimated by approximately 3.25 %, a characteristic associated with the *GGA* method. The strong agreement between the results of our

calculations and the experimental data indicates a high level of theoretical accuracy. The projected band structure and partial density of states *(PDOS)* were calculated using the *HSE03* hybrid functional and are illustrated in Figure 1d. Bulk *Te* exhibits a nearly direct band gap *(BG)* of 0.371 eV, located at the *H* points of the hexagonal first *Brillouin* Zone *(BZ)* (refer to Figure 1c). This *BG* value closely matches the experimental obtained value of 0.33 eV [39] and previous theoretical studies [40]-[43]. A notable feature of *Te DOS* is that the conduction band *(CB)* and the valence band (*VB*) are predominantly influenced by *p*-orbitals, which is a defining qualitative characteristic of *Te*'s electronic states.

One of the most significant characteristics of a material is its optical properties as they show how the material's interacts with electromagnetic radiation, especially visible light. The trigonal lattice of bulk tellurium exhibits significant uniaxial optical anisotropy. Consequently, the optical features of bulk *Te* are influenced by the incident light polarization relative to the *c*-axis and are assessed along the $\perp c$ and $\parallel c$ polarization axis. Figure 2 presents the calculated optical functions of bulk *Te*.

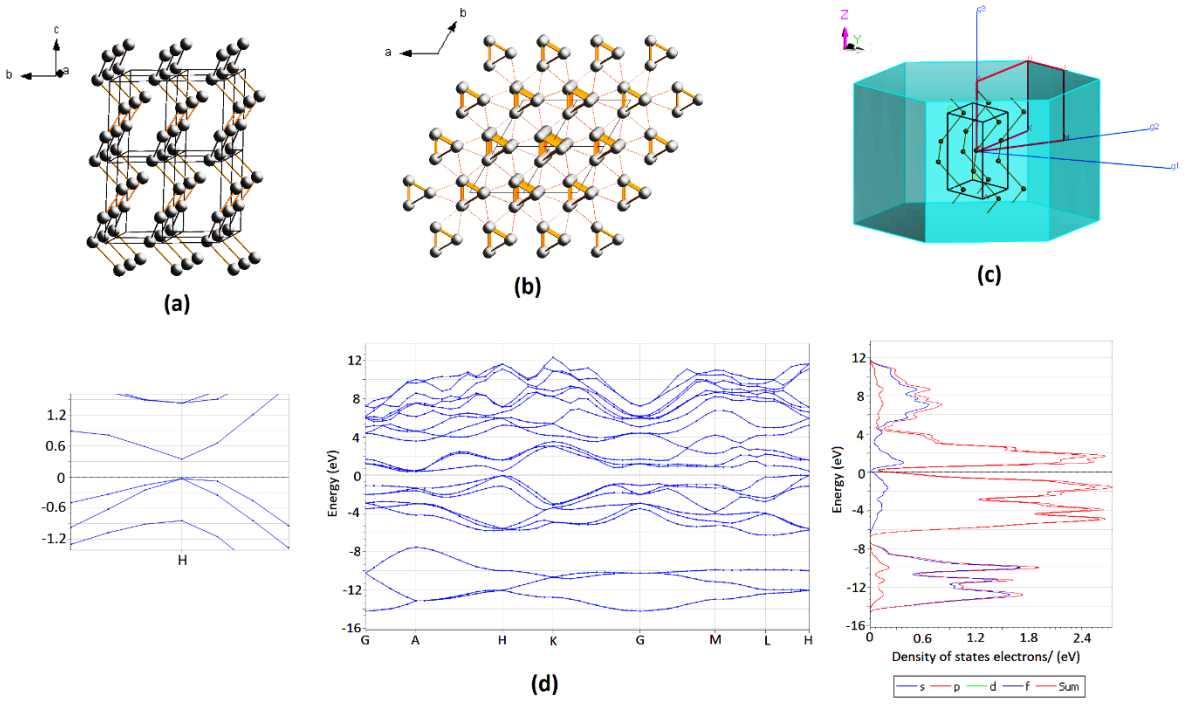

Figure 1: *Computed band structure and crystal of trigonal tellurium. (a) Crystal structure of Te arranged in spiral chains of tellurium atoms with covalent bonds. (b) View of tellurium atoms linked together via vdW inter-chain bonds along the c-axis with three-fold screw symmetry. (c) First Brillouin zone of Te with high-symmetry point. (d) Calculated band structure of Te located at the H points of the hexagonal first Brillouin Zone and the related partial density of states (PDOS). A zoomed-in view near the direct band edge at the H point is displayed in the left panel.*

The real and imaginary parts of the dielectric functions are illustrated in Figure 2a. The imaginary part *ε2(ω)* is directly associated with the energy band structure. The spectral dispersion along the $\perp c$ and $\parallel c$ polarization directions is irregular, attributed to the anisotropic nature of the tellurium crystal. The prominent peaks in the imaginary component *ε2(ω)* of *Te* along $\perp c$ *(and* $\parallel c$*)* are approximately at 1.95 eV (and 1.74 eV shifted to lower energy) with magnitudes of around 31.1 and 45.5. The static dielectric constant *ε1(0)* at zero photon energy, of *Te* along $\perp c$ *(and* $\parallel c$*)* (refer to Table 2), is about 28.6 (and 42.5), which closely matches the values observed by M. Cheng *et al.* [42], achieving a maximum at 28.8 and 43.2 for 0.813 and 0.757 eV, respectively. Tellurium in bulk exhibits nearly transparent properties; in the visible spectrum,

the reflectance of *Te* along ⊥ *c (and || c)* started at about 47% (and 45%) and increases to around 63.3% for 3.18 eV (and 70.9% for 3.11 eV). The reflectance drops to zero at energies higher than 20 eV (Figures 2b).

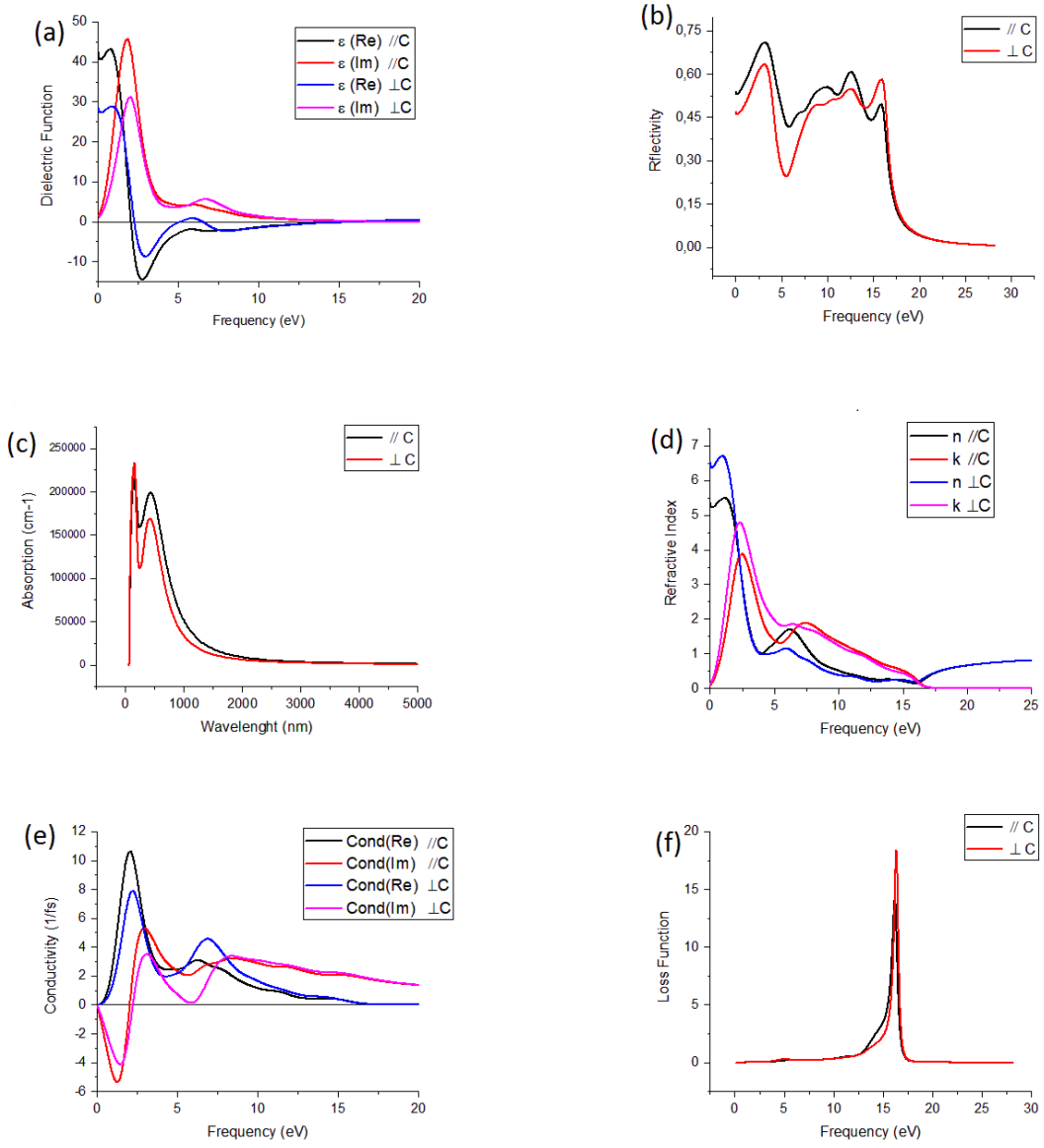

Figure 2: *Calculated optical properties of bulk Te along the ⊥ c and || c polarization axes: (a) The dielectric function, (b) The refractive index, (c) The optical conductivity, (d) Absorption spectra, (e) Reflectivity, and (f) Loss function plot.*

The optical absorption curve displays two separate peaks with an absorption edge in the ultraviolet, as seen in Figures 2c. At 1.69 and 2.34 x 10^{+5} cm^{-1} along ⊥ *c*, corresponding to 420 nm (2.95 eV) and 157 nm (8.08 eV), respectively, and along || *c* at 1.99 x 10^{+5} cm^{-1} and 2.16 x 10^{+5} cm^{-1}, corresponding to 436 nm (2.87 eV) and 149 nm (8.35 eV), respectively. The optical absorption curves in both orientations exhibit similar patterns with important absorption for Te, ranging from UV to IR revealing the great potential of Te in IR photo-detection [40], [44]. The refractive index, as functions of photon energy, are displayed in Figure 2d. The static refractive index *n(0)* of tellurium along ⊥ *c (and || c)* is around 5.35 (and 6.52), respectively, as shown in Table 2. It is higher in the infrared and progressively decreases in the visible and ultraviolet zones. *Te* crystal possesses a negative optic axis, as indicated by the calculated birefringence $\Delta n = ne - no$ = -1.17,

which is a measure of the variations in refractive indices that the material exhibits in different polarization directions. This value is less than the one reported by D. K. Sang *et al.* [40] as -2.06.

In contrast to the results obtained by P. Ghosh *et al.* [45], the optical conductivity $\sigma(\omega)$ of tellurium is somewhat shifted to higher energy in the visible region, along $\perp c$ (and $||$ *c)* (see Figure 2e) and increases and reaches maximum values at 2.21 eV (and 2.07 eV), respectively. The energy dissipation of a fast electron passing through is explained by the energy loss function, and its peak occurs at distinct incident light frequencies designed as the plasma frequency ωp. Referring to Figure 2f, the plasma frequencies of *Te* along $\perp c$ *(and* $||$ *c)* are approximately 14.3 (and 18.4) at 16.2 eV, respectively. This relates to the photon energy where reflectivity rapidly declines.

3.2 Electronic Microscopy

A typical *SEM* image in Figure 3a clearly shows that the products are *MTs* with imperfect rectangular and hexagonal cross-sections. They grow inclined at an angle of 30 - 48° to the substrate surface, with lengths ranging from 70 to 180 µm and an average value of approximately 130 µm, comparable to dimensions observed in *Te MTs* from different synthesis processes [19], [20], [25], and [46]. Figure 3b presents a *TEM* image of a fractured individual *MT*. The image contrast reveals a hollow cavity, indicating a tubular structure. The single-crystalline growth nature of the *MTs* along the *c*-axis is shown by the indexation of the selected area electron diffraction *(SAED)* pattern (inset) to the zone axis of trigonal *Te*. Additional spots in the diffracted pattern may be attributed to double diffraction. *XEDS* analysis indicated that the *MTs* consist of *Te* signals, while the substrate is a mixture of *Bi* (22.45%), *Te* (16.77%), and *I* (59.87%).

Powder diffraction *(XRD)* was performed to analyze the crystal structure and phase formation of the final product. Since the *MTs* were grown on a substrate, only the *XRD* pattern of substrate and *MTs* was feasible, as depicted in Figure 3c. An automated search using the software *Match3* [28] led to the identification of two phases: bismuth triiodide BiI_3 *(Entry # 96-810-4288)* and tellurium *Te (Entry # 96-900-8581)*. The diffracted peaks of *Te* correspond to the trigonal phase with parameters a = 4.4693 Å and c = 5.91492 Å, comparable with experimental values obtained (see Table 1). The stronger reflection *(101)* suggests preferential growth of *Te* along the *[0001]* direction [20], [25], and [46]. The remaining diffracted peaks in the *XRD* pattern belong to the trigonal phase of the substrate BiI_3 with lattice parameters a = 7.5160 Å and c = 20.7180 Å, exhibiting a preferred orientation along the *(113)* plane. This indicates that the substrate used for *Te MTs* growth is a mixture of BiI_3 and elemental *Te*. It is known that BiI_3 and its nanoparticles have a catalytic effect on semiconductor growth, nanomaterials, polymers, and more [47]-[50]. With matching symmetry between *Te* and BiI_3, it can be inferred that BiI_3 catalyzes not only the growth formation of *Te MTs* but can also promotes better epitaxial growth and alignment of the *MTs*.

Te MTs with imperfect hexagon-shaped cross-sections have outer diameters ranging from 32 to 73 µm; with an average value around 47 µm (refer to Figure 3a). The inner hole sizes range from 5 to 48 µm, with an average size of approximately 25 µm. The wall thickness of these *MTs* ranges from about 6.5 to 17.5 µm, with an average thickness around 12.5 µm, comparable to dimensions observed in *Te MTs* from different synthesis processes. High-magnification *SEM* images in Figure 4a display individual *Te MTs* with a hollow prismatic morphology and hexagonal cross-sections. Some images show deposited plate-like crystals on *MTs* surfaces, potentially acting as catalyst particles (Figure 4b). Additionally, unique *MTs* with obstructed holes are observed in Figures 4c and 4d.

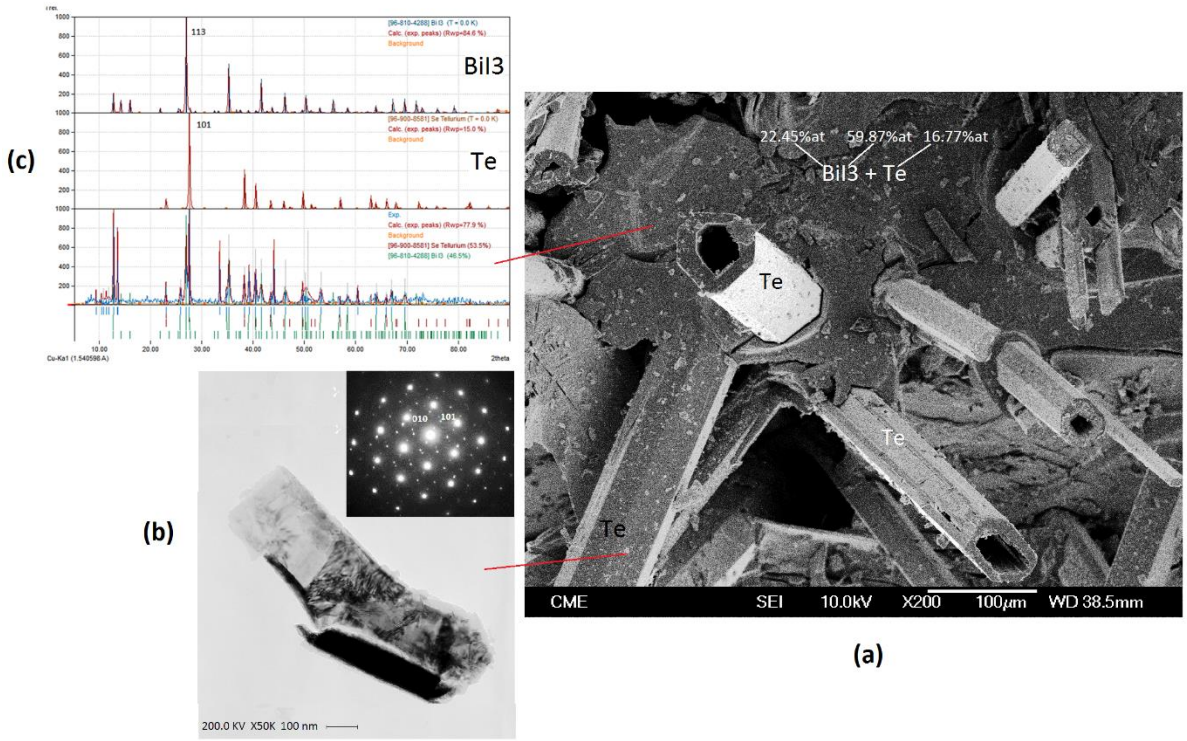

Figure 3: *(a) Lower-magnification SEM image capturing the Te MTs grown on a BiI_3 substrate. The image displays MTs morphologies with imperfect hexagonal and rectangular cross-sections. (b) Typical TEM image of a fractured individual MT, and inset the SAED pattern obtained along the [101] zone axis as indexed to the trigonal Te zone axis. (c) XRD patterns of Te MTs grown on a BiI_3 substrate. The XRD profile closely matches both trigonal bismuth triiodide BiI3 (Entry # 96-810-4288), and tellurium Te (Entry # 96-900-8581), identified through an automated search using Match3 software [54].*

Further high-magnification SEM images in Figure 4e and 4f reveal individual *MTs* with rectangular-shaped cross-sections ranging from approximately 9 to 29.5 µm x 29.5 to 45 µm, with wall thickness estimated at about 4 to 14.5 µm. Figures 4g and 4h depict an incomplete self-assembly of two *MTs* with hexagonal and rectangular cross-sections respectively, representing intermediate product during *MTs* growth. While *Te* nanotubes and *MTs* are typically produced with hexagonal or triangular cross-sections according to B. Mayers *et al.* and P. Mohanty *et al.* [15], [16], rectangular cross-sections, are less commonly observed in tellurium compared to other inorganic compounds such as *PbTe*, SnO_2, and CdI_2 doped by BiI_3 [51], [52]. Most *MTs* exhibit rough outer surfaces, and the exact mechanism behind their formation remains incompletely understood. An individual *MT* shown in Figure *4g* and *4h* displays an imperfectly closed end, offering insights into *MT* formation mechanisms. Earlier experimental findings indicate that in the preparation of Te *MTs*, the growth mechanisms typically involve nucleation and growth through a vapor-solid process [17]. The continuous deposition of Te nuclei onto trigonal- BiI_3 substrates through thermal evaporation leads to faster growth rates along the *[0001]* axes due to anisotropic structure of Te, promoting the formation of *Te* nanowires perpendicular to the substrate as reported by many authors [16], [25]-[27]. However, it remain unclear whether a correlation exists between the BiI_3 substrate structure and the morphology of the produced *MTs*.

The diameter and wall thickness of these *MTs* suggest that their walls likely form through the coalescence of adjacent individual nanowires, which tend to align parallelly and self-assemble via an oriented attachment process into complete microtubes. T. Siciliano *et al.* [26] and Y. Xia *et al.* [17] reported similar conclusions with synthesized Te *MTs* and *NTs*, respectively very closely to those reported during the formation of *ZnO* and PbI_2 *MTs* [53], [54]. This mechanism contrasts with tubular bismuth misfit structure, where tubes form through packing helical chains via vdW interactions [55].

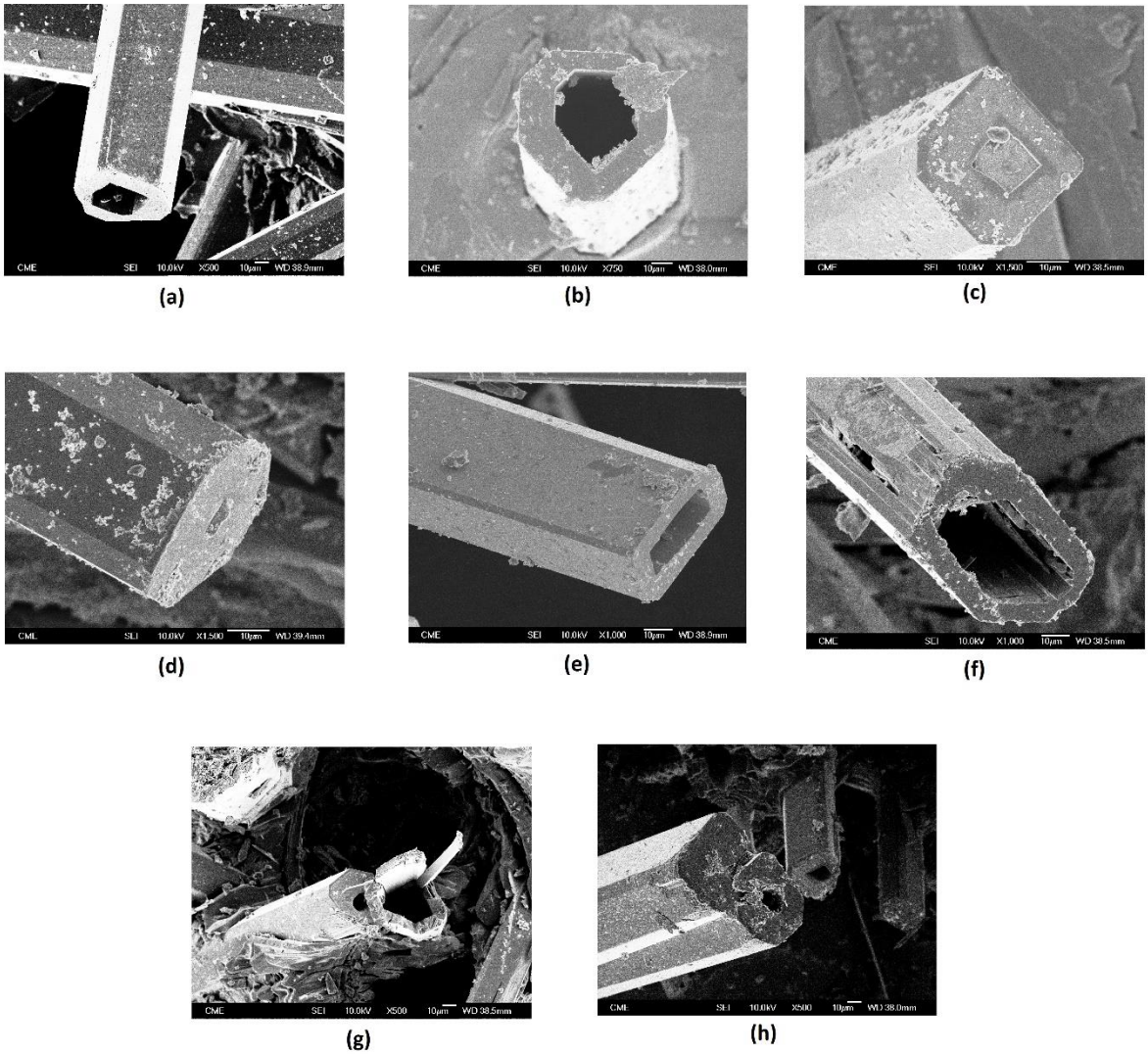

Figure 4: *(a) SEM images of individual Te MT displaying distinctive hollow prismatic morphology with hexagonal cross-section. (b) MTs with deposited plate-like-crystals. (c) and (d) distinctive MTs with obstructed holes. (e) and (f) SEM images of individual MTs with rectangular-shaped cross-section. (f) Present a MT imperfectly closed in one flank side. (g) and (h) show an incomplete self-assembly MTs.*

4 Conclusions

Crystalline *Te MTs* were obtained by chemical vapor transport process (CVT) using a stoichiometric mixture of *Bi*, *Nb*, and *Te* in the presence of iodine. Electron microscopy techniques (*SEM*, *EDS*, and *SAED*) and *X*-ray powder diffraction *(XRD)*; demonstrate that the *Te MTs* displayed a single-crystalline morphology with imperfect hexagonal and rectangular cross-sections. The *MTs* grow inclined at an angle of 30 – 48° to the BiI_3 substrate surface, with a diameter range of 32 to 73 µm and a length range of 70 to 180 µm and further observations suggest that the *Te MTs* formation results from the coalescence of adjacent individual nanowires. However, additional experimental synthesis of Te *MTs* on BiI_3-type substrates should be conducted in order to elucidate the role of the substrate on the morphology of the *MTs*. Based on *DFT* computing, the predicted band structure for bulk *Te* by *CASTEP* using the *HSE03* hybrid functional is about 0.371 eV, which is in close agreement with the experimental measurement of 0.33 eV. The optical properties of bulk *Te* are affected by the orientation of incident light polarization, attributed to the anisotropic nature of the Tellurium crystal. Bulk *Te* exhibits almost transparent characteristics and significant absorption in the UV, illustrating a highly promising candidate for optoelectronic applications, such as IR photodetection.

5 Declarations

5.1 Data Availability

The deposition number CCDC 2339727 contains the supplementary crystallographic data for this paper. These data can be obtained free of charge via www.ccdc.cam.ac.uk/conts/ retrieving.html (or from the Cambridge Crystallographic Data Centre, 12 Union Road, Cambridge CB2 1EZ, UK; fax: (+44) 1223-336-033; or deposit@ccdc.ca.ac.uk.

5.2 Competing Interests

There is no potential conflict of interest exists in this publication.

5.3 Publisher's Note

AIJR remains neutral with regard to jurisdictional claims in published institutional affiliations.

How to Cite this Article:

M. Kars, A. G. Herrero, and T. Roisnel, "Synthesis and Characterization of Tellurium Microtubes", *J. Mod. Mater.*, vol. 12, no. 1, pp. 7–17, Feb. 2025. https://doi.org/10.21467/jmm.12.1.7-17

References

[1] U. Coscia, G. Ambrosone, M. Palomba, S. Binetti, A. Le Donne, D. Siliqi, and G. Carotenuto. Photoconductivity of tellurium-poly (methyl methacrylate) in the ultraviolet-visible-near infrared range. *Applied Surface Science*, Vol 457, pp. 229-234, 2018. DOI : https://doi.org/10.1016/j.apsusc.2018.06.221

[2] D. Matteo, S. Y. Tochitsky and C. Joshi. Tellurium crystal pumped with ultrafast 10 µm pulses demonstrates a giant nonlinear optical response. *Optics Express*, Vol *31*(17), pp. 27239-27254, 2023. DOI : https://doi.org/10.1364/OE.497186

[3] S. Lin, W. Li, Z. Chen, J. Shen, B. Ge and Y. Pei. Tellurium as a high-performance elemental thermoelectric. *Nature communications*, Vol *7*(1), p.10287, 2016. DOI: https://doi.org/10.1038/ncomms10287

[4] L. Tao, Z. Jun-Wei, W. Dong-rui and D. Zhi-Min. Remarkable piezoresistance effect on the flexible strain sensor based on a single ultralong tellurium micrometre wire. *Journal of Physics D: Applied Physics*, Vol 47(50), p. 505103, 2014. DOI : https://doi.org/10.1088/0022-3727/47/50/505103

[5] D. Sári, A. Ferroudj, D. Semsey, H. El-Ramady, E. C. Brevik and J. Prokisch. Tellurium and Nano-Tellurium: Medicine or Poison? *Nanomaterials*, Vol 14(8), p.670, 2024. DOI: https://doi.org/10.3390/nano14080670

[6] A. Das and B. K. Banik. Semiconductor characteristics of tellurium and its implementations. *Physical Sciences Reviews*, Vol *8*(12), pp. 4659-4687, 2023. DOI : https://doi.org/10.1515/psr-2021-0108

[7] M. C. Zambonino, E. M. Quizhpe, F. E. Jaramillo, A. Rahman, N. Santiago Vispo, C. Jeffryes and S. A. Dahoumane. Green synthesis of selenium and tellurium nanoparticles: current trends, biological properties and biomedical applications. *International journal of molecular sciences*, Vol *22*(3), p. 989, 2021. DOI : https://doi.org/10.3390/ijms22030989

[8] V. Miranda La Hera, X. Wu, J. Mena, H. R. Barzegar, A. Ashok, S. Koroidov, T. Wågberg and E. Gracia-Espino. Controlled Synthesis of Tellurium Nanowires. *Nanomaterials*, Vol 12(23), p. 4137, 2022. DOI : https://doi.org/10.3390/nano12234137

[9] H. Zhu, L. Fan, K. Wang, H. Liu, J. Zhang and S. Yan. Progress in the Synthesis and Application of Tellurium Nanomaterials. *Nanomaterials*, Vol *13*(14), p. 2057, 2023. DOI : https://doi.org/10.3390/nano13142057

[10] D. Tsiulyanu. Gas sensing features of nanostructured tellurium thin films. *Beilstein Journal of Nanotechnology*, Vol 11(1), pp. 1010-1018, 2020. DOI : https://doi.org/10.3762/bjnano.11.85

[11] A. Kramer, M. L. Van de Put, C. L. Hinkle and W. G. Vandenberghe. Tellurium as a successor of silicon for extremely scaled nanowires: a first-principles study. *npj 2D Materials and Applications*, Vol 4(1), p. 10, 2020. DOI : https://doi.org/10.1038/s41699-020-0143-1

[12] A. Singh, J. S. Dhau, R. Kumar, R. Badru, and A. Kaushik. Exploring fluorescence properties of tellurium-containing molecules and their advanced applications. *Physical Chemistry Chemical Physics*, Vol 26, pp. 9816-9847, 2024. DOI: https://doi.org/10.1039/D3CP05740B

[13] C. Liu, R. Wang and Y. Zhang. Tellurium Nanotubes and Chemical Analogues from Preparation to Applications: A Minor Review. *Nanomaterials*, Vol *12*(13), p. 2151, 2022. DOI : https://doi.org/10.3390/nano12132151

[14] J. Li, Q. Yang, D. He, Y. Wang, E. Hwang, and Y. Yang. Morphology-controlled synthesis, growth mechanism, and applications of tellurium nanostructures. *Materials Advances*, Vol 5, pp. 7548-7560, 2024. DOI: https://doi.org/10.1039/d4ma00572d

[15] B. Mayers and Y. Xia. One-dimensional nanostructures of trigonal tellurium with various morphologies can be synthesized using a solution-phase approach. *Journal of Materials Chemistry*, Vol *12*(6), pp. 1875-1881, 2002. DOI : https://doi.org/10.1039/B201058E

[16] P. Mohanty, T. Kang, B. Kim, and J. Park. Synthesis of single crystalline tellurium nanotubes with triangular and hexagonal cross sections. *The Journal of Physical Chemistry B*, Vol *110*(2), pp. 791-795, 2006. DOI : https://doi.org/10.1021/jp0551364

[17] Y. Xia, P; Yang, Y. Sun, Y. Wu, B. Mayers, B. Gates, Y. Yin, F. Kim and H. Yan. One- dimensional nanostructures: synthesis, characterization, and applications. *Advanced materials*, Vol 15(5), pp. 353-389, 2003. DOI : https://doi.org/10.1002/adma.200390087

[18] J. W. Liu, J. Xu, W. Hu, J. L. Yang and S. H. Yu. Systematic synthesis of tellurium nanostructures and their optical properties: from nanoparticles to nanorods, nanowires, and nanotubes. *Chem Nano Mat*, Vol 2(3), pp. 167-170, 2016. DOI : https://doi.org/10.1002/cnma.201500206

[19] H. Zhu, L. Fan, K. Wang, H. Liu, J. Zhang and S. Yan. Progress in the Synthesis and Application of Tellurium Nanomaterials. *Nanomaterials*, 13(14), p. 2057, 2023. DOI : https://doi.org/10.3390/nano13142057

[20] H. Zhu, H. Zhang, J. Liang, G. Rao, J. Li, G. Liu, Z. Du, H. Fan and J. Luo. Controlled synthesis of tellurium nanostructures from nanotubes to nanorods and nanowires and their template applications. *The Journal of Physical Chemistry C*, Vol 115(14), pp. 6375-6380, 2011. DOI : https://doi.org/10.1021/jp200316y

[21] G. Qiu, A. Charnas, C. Niu, Y. Wang, W. Wu and P. D. Ye. The resurrection of tellurium as an elemental two-dimensional semiconductor. *npj 2D Materials and Applications*, Vol 6(1), p. 17, 2022. DOI : https://doi.org/10.1038/s41699-022-00293-w

[22] X. Zhao, J. Shi, Q. Yin, Z. Dong, Y. Zhang, L. Kang, Q. Yu, C. Chen, J. Li, X. Liu and K. Zhang. Controllable synthesis of high-quality two-dimensional tellurium by a facile chemical vapor transport strategy. *I Science*, Vol 25(1). 2022. DOI : https://doi.org/10.1016/j.isci.2021.103594

[23] A. Chen, S. Ye, Z. Wang, Y. Han, J. Cai and J. Li. Machine-learning-assisted rational design of 2D doped tellurene for fin field-effect transistor devices. *Patterns*, *4*(4), 2023. DOI : https://doi.org/10.1016/j.patter.2023.100722

[24] T. Zhu, Y. Zhang, X. Wei, M. Jiang and H. Xu. The rise of two-dimensional tellurium for next-generation electronics and optoelectronics. *Frontiers of Physics*, Vol 18(3), p. 33601, 2023 DOI : https://doi.org/10.1007/s11467-022-1231-9

[25] A. M. Qin, Y. P. Fang, and C. Y. Su. One-step fabrication of selenium and tellurium tubular structures. *Inorganic Chemistry Communications*, Vol 7(9), pp. 1014-1016, 2004. DOI : https://doi.org/10.1016/j.inoche.2004.07.003

[26] T. Siciliano, E. Filippo, A. Genga, G. Micocci, M. Siciliano, and A. Tepore. Tellurium microtubes synthesized by thermal evaporation method. *Crystal Research and Technology*, Vol 46(8), pp. 765-768, 2011. DOI : https://doi.org/10.1002/crat.201000578

[27] J. Lu, Y. Xie, F. Xu and L. Zhu. Study of the dissolution behavior of selenium and tellurium in different solvents—a novel route to Se, Te tubular bulk single crystals. *Journal of Materials Chemistry*, Vol 12(9), pp. 2755-2761, 2002. DOI : https://doi.org/10.1039/B204092A

[28] Phase Analysis using Powder Diffraction, Version 3.x, Crystal Impact - Dr. H. Putz & Dr. K. Brandenburg GbR, Kreuzherrenstr. 102, 53227 Bonn, Germany, https://www.crystalimpact.de/match

[29] Bruker (2006). APEX2, SAINT, Bruker AXS Inc., Madison, Wisconsin, USA 2006.

[30] G. M. Sheldrick. Program for the refinement of crystal structures. SADABS, Bruker AXS Inc., Madison, Wisconsin, USA 2002. http:// shelx.uni-ac.gwdg.de/shelx/

[31] L. Palatinus and G. Chapuis. SUPERFLIP-a computer program for the solution of crystal structures by charge flipping in arbitrary dimensions. *Journal of Applied Crystallography*, Vol 40, pp. 786-790, 2007. DOI : https://doi.org/10.1107/S0021889807029238

[32] V. Petříček, M. Dušék and L. Palatinus. The crystallographic computing system. JANA, 2006 Institute of Physics, Praha, Czech Republic, 2006. http://www-xray.fzu.cz

[33] K. Brandenburg and H. Putz. (2006). Diamond. Crystal Impact GbR, Bonn, Germany. http://www.crystalimpact.de

[34] S. J. Clark, M. D. Segall, C. J. Pickard, P. J. Hasnip, M. I. Probert, K. Refson, M. C. Payne. First principles methods using CASTEP. *Zeitschrift für kristallographie-crystalline materials*, Vol 220(5-6), pp. 567-570, 2005. DOI : https://doi.org/10.1524/zkri.220.5.567.65075

[35] *Materials Studio CASTEP Manual © Accelrys*, 2010. http://www.tcm.phy.cam.ac.uk/castep/documentation/WebHelp/CASTEP.html.

[36] L. Kleinman and D. M. Bylander. Efficacious form for model pseudopotentials. *Physical Review Letters*, Vol 48(20), p. 1425, 1982. DOI : https://doi.org/10.1103/PhysRevLett.48.1425

[37] J. Heyd and G. E. Scuseria. Assessment and validation of a screened Coulomb hybrid density functional. *The Journal of chemical physics*, Vol 120(16), pp. 7274-7280, 2004. DOI: https://doi.org/10.1063/1.1668634

[38] C. Adenis, V. Langer and O. Lindqvist. Reinvestigation of the structure of tellurium. Acta Crystallographica Section C: Crystal Structure Communications, Vol 45(6), pp. 941-942, 1989. DOI: https://doi.org/10.1107/S0108270188014453

[39] V. B. Anzin, M. I. Eremets, Y. V. Kosichkin, A. I. Nadezhdinskii, and A. M. Shirokov. Measurement of the energy gap in tellurium under pressure. *physica status solidi (a)*, Vol 42(1), pp. 385-390, 1977. DOI : https://doi.org/10.1002/pssa.2210420143

[40] D. K. Sang, B. Wen, S. Gao, Y. Zeng, F. Meng, Z. Guo and H. Zhang. Electronic and optical properties of two-dimensional tellurene: from first-principles calculations. *Nanomaterials*, Vol 9(8), p. 1075, 2019. DOI : https://doi.org/10.3390/nano9081075

[41] M. Cheng, S. Wu, Z. Z. Zhu and G. Y. Guo. Large second-harmonic generation and linear electro-optic effect in trigonal selenium and tellurium. *Physical Review B*, Vol 100(3), p. 035202, 2019. DOI: https://doi.org/10.1103/PhysRevB.100.035202

[42] M. Cheng, Z. Z. Zhu and G. Y. Guo. Strong bulk photovoltaic effect and second-harmonic generation in two-dimensional selenium and tellurium. *Physical Review B*, Vol 103(24), p. 245415, 2021. DOI: https://doi.org/10.1103/PhysRevB.103.245415

[43] V. G. Orlov and G. S. Sergeev. . Electronic band structure and chemical bonding in trigonal Se and Te. *AIP Advances*, Vol 12(5), 2022. DOI: https://doi.org/10.1063/5.0087880

[44] J. Zha, D. Dong, H. Huang, Y. Xia, J. Tong, H. Liu, H. P. Chan, J. C. Ho, C. Zhao, Y. Chai and C. Tan. Electronics and Optoelectronics Based on Tellurium. *Advanced Materials*, Vol 36, p. 2408969, 2024. DOI: https://doi.org/10.1002/adma.202408969

[45] P. Ghosh, M. U. Kahaly and U. V. Waghmare. Atomic and electronic structures, elastic properties, and optical conductivity of bulk Te and Te nanowires: A first-principles study. *Physical Review B*, Vol 75(24), p. 245437, 2007. DOI: https://doi.org/10.1103/PhysRevB.75.245437

[46] K. W. Song, J. H. Bae, H. K. Kim, T. H. Kim, M. H. Park and C. W. Yang. Fabrication of CdTe/Te Hetero-Nanostructures by Vapor-Solid Process. *Journal of Nanoscience and Nanotechnology*, Vol 11(7), pp. 6559-6562, 2011. DOI : https://doi.org/10.1166/jnn.2011.4410

[47] X. Lv, F. L. Y. Lam, and X. Hu. A review on bismuth oxyhalide (BiOX, X= Cl, Br, I) based photocatalysts for wastewater remediation. *Frontiers in Catalysis*, Vol 2, p. 839072, 2022. DOI : https://doi.org/10.3389/fctls.2022.839072

[48] R. Zhuang, S. Cai, Z. Mei, H. Liang, N. Zhao, H. Mu, W. Yu, Y. Jiang, J. Yuan, S. Lau and S. Deng. Solution-grown BiI/BiI3 van der Waals heterostructures for sensitive X-ray detection. *Nature Communications*, Vol 14(1), p. 1621, 2023. DOI : https://doi.org/10.1038/s41467-023-37297-z

[49] L. Bethencourt, I. Aguiar, M. Pérez Barthaburu, D. Oreggioni, R. Costa de Santana, L. J. Queiroz Maia and L. Fornaro. From a novel synthesis method for bismuth tri-iodide nanoparticles to a solution-processed hybrid material: BiI3-conducting polymer. *Journal of Materials Science*, Vol 57(37), pp.17592-17608, 2022. DOI : https://doi.org/10.1007/s10853-022-07703-w

[50] F. Arjmand, Z. Golshani, S. J. Fatemi, S. Maghsoudi, A. Naeimi and S. M. A. Hosseini. The lead-free perovskite solar cells with the green synthesized BiI3 and AgI nanoparticles using Vitex agnus-castus plant extract for HTM-free and carbon-based solar cells. *Journal of Materials Research and Technology*, Vol 18, pp. 1922-1933, 2022. DOI : https://doi.org/10.1016/j.jmrt.2022.03.088

[51] J. Hu, Z. Chen, H. Jiang, Y. Sun, Y. Bando and D. Golberg. Rectangular or square, tapered, and single-crystal PbTe nanotubes. *Journal of Materials Chemistry*, Vol 19(19), pp. 3063-3068, 2009. DOI : https://doi.org/10.1039/B822303C

[52] I. M. Bolesta, I. N. Rovetskyj, I. D. Karbovnyk, and M. V. Partyka. Formation of microtubes in CdI_2 crystals doped with BiI_3. *Technical Physics Letters*, Vol 39, pp. 463-465, 2013. DOI : https://doi.org/10.1134/S1063785013050180

[53] J. S. Jeong, J. Y. Lee, J. H. Cho, H. J. Suh and C. J. Lee. Single-crystalline ZnO microtubes formed by coalescence of ZnO nanowires using a simple metal-vapor deposition method. *Chemistry of materials*, Vol 17(10), pp. 2752-2756, 2005. DOI : https://doi.org/10.1021/cm049387l

[54] G. Zhu, M. Hojamberdiev, P. Liu, J. Peng, J. Zhou, X. Bian and X. Huang. The effects of synthesis parameters on the formation of PbI_2 particles under DTAB-assisted hydrothermal process. *Materials Chemistry and Physics*, Vol 131(1-2), pp. 64-71, 2011. DOI : https://doi.org/10.1016/j.matchemphys.2011.07.010

[55] A. Gómez -Herrero, A. R. Landa-Canovas, S. Hansen and L. C. Otéro- Diáz. Electron microscopy study of tubular crystals $(BiS)_{1+\delta}(NbS_2)_n$. *Micron*, Vol 31(5), pp. 587-595, 2000. DOI : https://doi.org/10.1016/S0968-4328(99)00141-9